Energy 338 (2025) 138880

Contents lists available at ScienceDirect

Energy

journal homepage: www.elsevier.com/locate/energy

# Development, dynamic analysis, and experimental evaluation of a hybrid wave-tidal energy converter featuring nonlinear dual inputs

Peihao Chen [a], Dawei Wu [a,b,*], Yiqing Yang [c], Yan Zhang [a], Athanasios Tsolakis [a], Karl Dearn [a]

[a] Department of Mechanical Engineering, University of Birmingham, Birmingham, B15 2TT, United Kingdom
[b] Department of Engineering, Durham University, Durham, DH1 3LE, United Kingdom
[c] School of Mechanical Engineering and Automation, Beihang University, Beijing 100191, China

ARTICLE INFO

Handling Editor: Prof G Iglesias

*Keywords:*
Multi-energy complementary
Wave energy converter
Tidal energy converter
Discretization modeling
Nonlinear dynamics

ABSTRACT

Current hybrid wave–tidal energy conversion technologies remain inadequate in fully leveraging the complementarity between wave and tidal energy, limiting overall efficiency and output stability. Moreover, conventional modeling approaches rely on idealized continuous sinusoidal wave inputs, making them unsuitable for capturing real ocean conditions or performing time-domain analysis. To address these gaps, this study proposes a hybrid wave-tidal energy converter (HWTEC) featuring a nonlinear motions rectification and coupling device (NLMRCD). Within the NLMRCD, a mechanical motion rectifier (MMR) converts reciprocating wave motion into unidirectional rotation, mitigating energy loss from frequent motion reversals. A bevel gearbox with one-way clutches couples wave and tidal energy inputs, enhancing power continuity and increasing voltage output. A novel discretization modeling methodology is developed to characterize the nonlinear interaction between wave and tidal modules. It accepts discrete input data and automatically identifies overrunning phases, simplifying time-domain calculations without requiring continuous input functions. Simulations under ocean-like conditions yield a peak power output of 18.72 W and an efficiency of 60.94 %. Experimental validation on a custom dual-input test bench confirmed these results, achieving 19.65 W and 61.34 %, respectively. The NLMRCD enhances output power and voltage stability by coupling intermittent wave and tidal energy, thereby improving system usability and conversion efficiency. The proposed discretization modeling approach overcomes limitations of continuous inputs in traditional methods, and offers a robust framework for simulation using measured wave data.

## 1. Introduction

Renewable energy development is crucial for achieving global net-zero emissions. Hybrid energy conversion technologies that integrate and optimize multiple renewable energy sources offer distinct advantages over single-source systems. In the ocean, where high-density resources such as solar, geothermal, wind, tidal, and wave energy coexist, hybrid systems demonstrate even greater potential. Roy et al. [1] note that ocean-based hybrids can boost regional energy output, stabilize intermittent power, enhance reliability, and reduce infrastructure costs through shared systems and lighter equipment, making them more efficient and economical than separate solutions.

Wave, tidal, and wind energy are the three primary mechanical energy sources with high energy density and accessibility. Among them, wave and tidal energy are particularly promising due to their greater availability, elevated power density, and vast reserves [2], estimated at over 800 TWh/year and 8000 TWh/year globally, respectively [3]. The low variability, gradual changes, and high consistency of wave energy enable Wave Energy Converters (WEC) to operate up to 90 % of the time, significantly exceeding the 20 %∼30 % operational availability typical of wind power [4]. A comparative analysis of various renewable energy combinations [5] confirms the value of wave energy continuity. Tidal energy, in particular, offers high predictability with rarely affected by weather conditions [6]. Furthermore, the energy densities of wave and tidal energy are several times higher than wind energy [7], due to the density difference between water and air [8]. Tidal energy conversion is also considered relatively mature and reliable in marine environments [9]. Consequently, hybrid wave-tidal energy conversion is emerging as a

* Corresponding author. Department of Engineering, Durham University, Durham DH1 3LE, United Kingdom
*E-mail address:* dawei.wu@durham.ac.uk (D. Wu).

https://doi.org/10.1016/j.energy.2025.138880
Received 27 April 2025; Received in revised form 12 June 2025; Accepted 10 October 2025
Available online 11 October 2025

promising direction for advancing ocean renewable energy.

Global deployment and multi-system coordination of hybrid ocean energy conversion systems are discussed at the macro level in Ref. [10], where hybrid wave-tidal energy converters (HWTECs) are identified as relatively immature. The development of Wave Energy Converters (WEC) reported in Refs. [11–13] and Tidal Energy Converters (TEC) in Refs. [14,15] forms the technical foundation for hybrid wave-tidal energy conversion systems. Roy et al. [1] noted that wave energy conversion remains less mature than other renewable technologies, resulting in fewer hybrid wave-tidal energy projects compared to other hybrid configurations. Chen and Wu [2] offer a comprehensive review covering HWTEC design, implementation, modeling, and experimental methodologies, identifying strengths and limitations of existing approaches, and suggesting future directions, particularly in device design and modeling methodology.

Specifically, HWTECs can be broadly categorized into non-coupling and coupling types based on the degree of interaction between wave and tidal energy capture modules [2]. Non-coupling HWTECs either alternate between modules or integrate independently operating components without interaction. Examples include the hydro-kite system by Yin et al. [16], the oscillating buoy and vertical-axis turbines hybrid by Silva et al. [17], and the oscillating water column module and overtopping module hybrid by Calheiros-Cabral et al. [18]. In contrast, coupling HWTECs improve performance through interactive integration of energy capture modules. For instance, the systems developed by Jiang et al. [19,20] and Chen et al. [21,22] use a mechanical motion rectifier to couple inputs from wave and tidal currents, selecting the higher-speed input to stabilize output. Similarly, Park et al. [23] couples a horizontal cylinder and swing plate. The muti degree-of-freedom (DOF) hybrid system proposed by Cheng et al. [24] integrates oscillating wave surge converters with buoys to extend working stroke and boost power output. Other studies [25,26] show that proper motion synthesis, speed selection, and resonance in coupled systems can enhance output power and stability. However, many coupling strategies prioritize the dominant input, often neglecting lower-power contributions. Although multi-DOF systems broaden operating bandwidth, single-DOF designs are often more efficient [27]. Furthermore, the complementary time-scale characteristics of wave and tidal energy, which can effectively enhance the lower limit of output, remain underutilized. Consequently, current HWTEC designs face limitations in fully leveraging wave-tidal time-scale distribution complementary for optimal energy conversion.

With the development of ocean energy, multi-objective optimization methods have been applied to the assessment of wave energy flux [28], the improvement of energy converters [29,30], and the deployment optimization of multiple energy converters [31]. In terms of modeling method, nonlinear modeling methods can more accurately capture complex dynamics than linear approaches. A comprehensive review of such methods for hybrid wave-tidal systems is provided in Ref. [2]. Deriving the continuous kinetic equation of the buoy remains necessary in Ref. [32] for carrying out the subsequent dynamic analysis. Existing models reported in Refs. [33–35] often rely on idealized continuous sinusoidal inputs, enabling nonlinear behaviors to appear repeatable. This repeatability enables the use of piecewise functions to differ the linear and nonlinear stages, simplifying the solution process. In contrast, modeling in Ref. [36] incorporate variable inertia, leading to a more complex, nonlinear velocity response that resists expression as explicit functions. These approaches depend on idealized continuous input functions, which do not reflect the randomness and unpredictability of real ocean waves. There is growing interest in using real wave data as input. High-fidelity output of the real-time heave motion of devices is achieved in a wave tank [37] by measuring the incident wave height. When real wave data are introduced into simulations, the output becomes much more complex to calculate. Furthermore, most models neglect the coupling effects between wave and tidal modules, despite the increasing recognition of such interactions in hybrid systems. Discretization is a fundamental approach in finite element simulations and is crucial for accurately modeling the dynamic behavior of tidal currents and waves [38]. It has been applied in tidal energy distribution studies grounded in hydrodynamic modeling [39], and has proven effective in enhancing tidal turbine performance for energy capture optimization [40]. However, its application remains limited in wave and tidal energy conversion research grounded in classical mechanics [41]. To address above limitations, a global discretization dynamic modeling method that incorporates both nonlinear responses and the modules coupling effects under realistic ocean conditions is urgently needed.

Dry lab testing plays a critical role for validating design concepts and modeling approaches, especially in the early development stages. Servo-hydraulic testing machines, which provide reciprocating motion through basic speed control, are commonly used in single wave energy converter studies [42]. For tidal energy converters (TECs), test benches based on servo motors and sensors have also been developed [43]. However, HWTEC systems demand more advanced testing setups. Specifically, two independent drive units are needed to emulate the reciprocating or irregular motion of waves and the continuous rotation of tidal turbines, along with torque and force sensors placed before and after the motion coupling [41]. Despite these technical requirements, there is a notable lack of mature testing platforms capable of integrating all necessary functions for HWTEC evaluation.

In summary, most current HWTEC designs insufficiently couple wave and tidal energy, limiting the full utilization of their complementary thus reducing output power and stability. Additionally, most modeling methods rely on continuous sinusoidal input assumptions, rendering them unsuitable for nonlinear cases and real ocean conditions. To address these issues, enhancing output power while stabilizing voltage, a HWTEC featuring a nonlinear motion rectification and coupling device is designed in this study. A time-domain discretization modeling method is proposed to accommodate realistic wave input profiles. A custom dual-input test bench is built to validate the modeling approach and evaluate device performance. The rest of the paper is structured as follows: Section 2 presents the HWTEC system design and operating principles, Section 3 covers the discretization modeling methods and simulation results, Section 4 and Section 5 detail the dual-input test bench setup and analyze experimental findings, respectively, and Section 6 provides the conclusion.

## 2. System design

To improve wave energy capture, stabilizing the front-end output can have a positive impact, though its effect on energy quality enhancement remains limited. Coupling stabilized wave energy with tidal energy leverages their complementary nature, increasing output power, reducing intermittency, and enabling the system to benefit from tidal grid-stabilization techniques. This integration helps smoothen the fluctuations of hybrid wave-tidal output, enabling grid connection with little imposing additional burden. Therefore, the HWTEC based on the Non-Linear Motions Rectification and Coupling Device (NLMRCD) is proposed, combining wave energy rectification, stabilization, and wave-tidal coupling.

### 2.1. Overall design

The HWTEC consists of an anchor, a waterproof case with a yawing plate, a buoy module, a horizontal-axis turbine, the NLMRCD, and a generator with essential circuitry (Fig. 1). The anchor and waterproof case serve as structural support and protect key components from seawater corrosion. The yawing plate passively orients the system with tidal currents to maximize tidal energy capture. Wave energy is primarily extracted from the vertical heave motion of surface water, while tidal energy originates from the periodic horizontal flow of deeper seawater [1]. Notably, their available powers are respectively proportional to the square of wave height and the cube of tidal current velocity. Limiting wave energy capture to a single degree of freedom has been

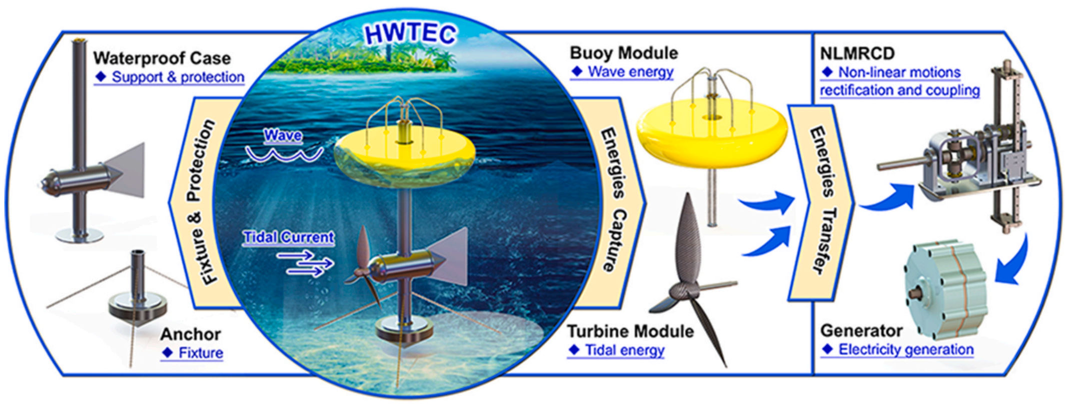


**Fig. 1.** Hybrid Wave-Tidal Energy Converter (HWTEC) based on Non-Linear Motions Rectification and Coupling Device (NLMRCD).

shown to significantly improve conversion efficiency [27]. Therefore, this system adopts a buoy for wave energy capture and a horizontal-axis turbine for tidal energy. The buoy module and horizontal-axis turbine are connected to the two input shafts of the NLMRCD via sliding bearings with sealing rings and a non-contact coupling mechanism, respectively. These components harness wave and tidal energy individually, which are then mechanically rectified and coupled by the NLMRCD. The resulting combined motion drives the generator through an output shaft, enabling continuous and optimized power generation.

### *2.2. Non-Linear Motions Rectification and Coupling Device (NLMRCD)*

The NLMRCD is designed based on the pinion-rack mechanical motion rectifier (MMR) and the bevel gear box with one-way clutches (Fig. 2).

Named for its similarity to an electrical rectifier, the MMR is designed to convert reciprocating motion, like the heaving motion of waves, into unidirectional motion, minimizing energy loss from frequent directional switches. Two gears with one-way clutches mounted in their central holes, referred to as one-way gears, engage unidirectionally with racks connected to the buoy. When the buoy module moves upward (Fig. 2a), one-way gear #1 rotates counterclockwise and engages with input shaft #1, while one-way gear #2 rotates clockwise and disengages. Conversely, during downward motion (Fig. 2b), one-way gear #2 engages input shaft #1 counterclockwise, while one-way gear #1 disengages. This configuration enables input shaft #1 to maintain a constant

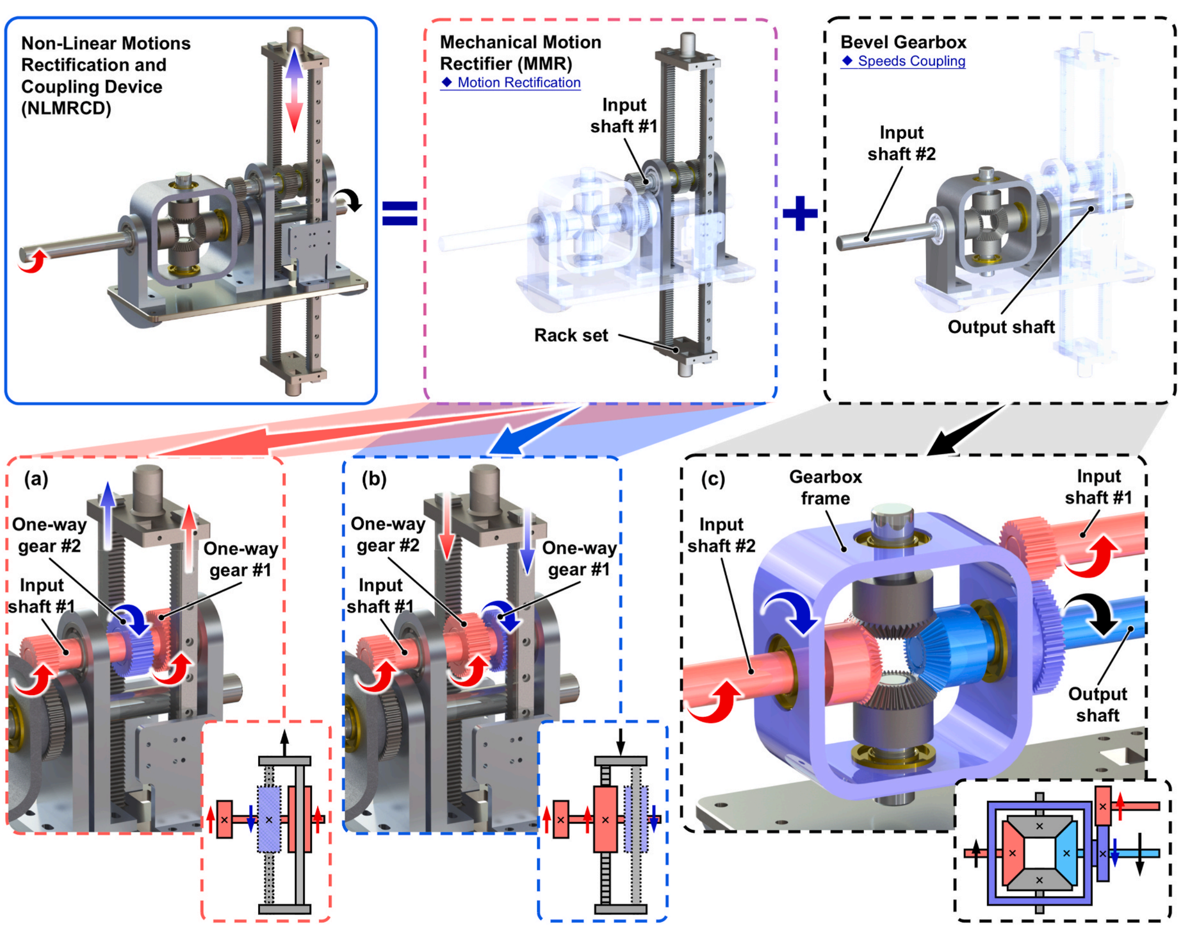


**Fig. 2.** Design of the motions rectification and coupling device.

counterclockwise rotation, thus achieving rectification of the reciprocating motion from waves. Additionally, both one-way gears engage in the same rotational direction, permitting input shaft #1 to overrun or rotate faster than the one-way gears when driven by momentum alone. This overrunning effect, similar to the freewheeling motion in cycling, occurs when the driving torque from the gears sharply decreases, allowing input shaft #1 to continue rotating thus reducing intermittent.

The bevel gearbox integrates the unidirectional rotation of the MMR with the one-way rotation of the tidal turbine, enabling effective mechanical coupling (Fig. 2c). One-way clutches operate similarly to directional valves, preventing the rotation of turbine from counteracting the rectified component of the reciprocating motion. The turbine is configured to drive input shaft #2, with the corresponding input bevel gear rotating counterclockwise. The relative rotation between the gearbox frame and the input bevel gear results in the output shaft speed equal to the sum of their individual speeds, thereby realizing the coupling and complementarity of speeds and mitigating the energy fluctuations typically observed in single-source wave or tidal energy converters. Specifically, if the transmission ratio between input shaft #1 and the gear box is $n$:1, the relative speed proportion between the two input shafts will be $(2/n)$:1 in the summation during linear phase, represented as $\omega_{out} = (2/n)|\omega_1| + |\omega_2|$, where $\omega_1$, $\omega_2$ and $\omega_{out}$ are the angular velocities of input shaft #1, input shaft #2 and output shaft, respectively. Here, the transmission ratio of 2:1 is adopted.

## 3. Discretization modeling

### 3.1. Methodology

In previous studies, acceleration function is typically obtained by differentiating the velocity function based on the continuity equation, which requires recalculation of global velocity and acceleration at each stage. However, with the incorporation of the overrunning phase and variable damping, the acceleration now depends on both the input force and the current motion state of the driven components. This nonlinearity renders analytical solutions difficult, necessitating manual evaluation.

In simulation software, the continuity equation is solved by discretizing it into small increments and computing it at each data point. When the step size is sufficiently small and the number of data points is adequate, the system can be accurately represented as accurate digital model, particularly in ocean wave and tidal scenarios, where variations are gradual and frequencies are low. Therefore, in the discretization modeling, it is reasonable to discretize the input velocity function into numerous data points with a time increment of $\Delta t$ [41]. Each pair of adjacent data points, $v_{(n)}$ and $v_{(n-1)}$, is treated as a small linear function, with the slope between them representing the input acceleration $a_{(n)}$. A crucial premise is that the driven and driving components share the same velocity and acceleration at the initial time, meaning no overrunning occurs between $v_{(1)}$ and $v_{(2)}$ - a condition that is indeed.

To explain the modeling logic, Fig. 3 illustrates the energy flow routes and the boundary conditions of the overrunning phase. The reciprocating linear motion $v_w$ of the buoy under wave action is converted into unidirectional rotation $\omega_{in1}$ by the pinion-rack MMR. During the overrunning phase, input shaft #1 rotates faster than the one-way gears; consequently, the intermediate variable $\omega'_{in1}$ is introduced as the input angular velocity to the wave-driven components, which is equal to $\omega_{in1}$ during the meshing phase and lower than $\omega_{in1}$ in the overrunning phase. $M_{in1}$ and $M_{d1}$ are the input torque and damping torque acting on the one-way gears, respectively, while $J_1$ denotes the equivalent moment of inertia of wave-driving components. Additionally, the intermediate variable $M_{mid}$ is introduced as the torque transmitted from one-way gears to input shaft #1, with $M_{d3}$ as the damping torque on input shaft #1 and $J_3$ as the equivalent moment of inertia of wave-driven components. In tidal-driving components, $\omega_{in2}$ is the input angular velocity of the tidal turbine. And the output angular velocity $\omega_{out}$ of the NLMRCD drives the generator.

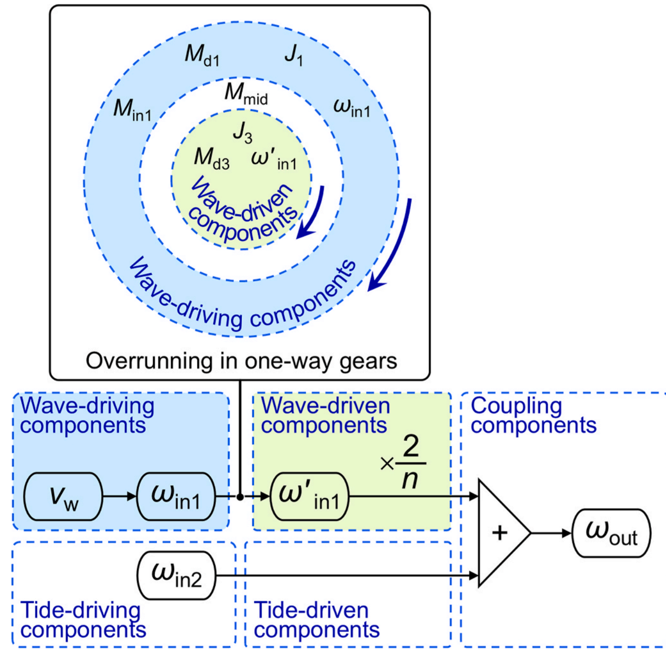


Fig. 3. Diagram of modeling logic and overrunning phase boundary conditions.

### 3.2. Boundary conditions

It is evident that during the meshing phase, the angular velocities and accelerations of the wave-driving and wave-driven components are identical. At the boundary transitioning into the overrunning phase, the acceleration of the wave-driving components begins to decrease, becoming lower than that of the wave-driven components, while their angular velocities remain equal to each other. As the overrunning phase progresses, both the acceleration and angular velocity of the wave-driving components fall below those of the wave-driven components. However, the acceleration of the wave-driving components gradually increases until it surpasses that of the wave-driven components. At the transition back into the meshing phase, the acceleration of the wave-driven components abruptly synchronizes with that of the wave-driving components, indicating the re-engagement of the one-way clutches. Simultaneously, their angular velocities also equalize. In the subsequent meshing phase, both accelerations and angular velocities rise synchronously, continuing the cyclic pattern. Therefore, the boundary conditions can be summarized as,

$$\begin{cases} M_{mid} > 0 \\ \dfrac{M_{in1} - M_{mid} - M_{d1}}{J_1} = \dfrac{M_{mid} - M_{d3}}{J_3} \\ \omega_1 = \omega_1' \end{cases} \xrightarrow{\text{Enter Overrunning}} \begin{cases} M_{mid} = 0 \\ \dfrac{M_{in1} - M_{d1}}{J_1} < \dfrac{-M_{d3}}{J_3} \\ \omega_1 = \omega_1' \end{cases} \tag{1}$$

$$\begin{cases} M_{mid} = 0 \\ \dfrac{M_{in1} - M_{d1}}{J_1} > \dfrac{-M_{d3}}{J_3} \\ \omega_1 < \omega_1' \end{cases} \xrightarrow{\text{Exit Overrunning}} \begin{cases} M_{mid} > 0 \\ \dfrac{M_{in1} - M_{mid} - M_{d1}}{J_1} = \dfrac{M_{mid} - M_{d3}}{J_3} \\ \omega_1 = \omega_1' \end{cases} \tag{2}$$

In Eqs. (1) and (2), angular velocity and acceleration share a common variable, damping, rendering them interdependent, which complicates the calculation of continuous functions necessary for obtaining numerical solutions. However, by discretizing the input velocity into data points in this study, the angular velocities and accelerations at each point can be calculated sequentially. Specifically, the angular velocity $\omega'_{(1)}$ at time $t_{(1)}$ is used to derive the acceleration $\alpha_{(1)}$ and damping torque $M_{d1(1)}$. Subsequently, $\alpha_{(1)}$ and $M_{d1(1)}$ are used to compute the angular velocity $\omega'_{(2)}$ at time $t_{(2)}$ (Fig. 4). Although this process incurs a misalignment error of a time step $\Delta t$, it significantly simplifies the solution process, allowing it to be automatically solved within the simulation program. Simulations and comparisons conducted based on a previous wave energy converter in Ref. [42] validated that with a time step $\Delta t$ of 0.001 s, the misalignment error remains within 0.5 %.

The torque balance of the HWTEC is established based on Newton's Second Law of Motion as follows,

$$\begin{cases} M_{in1} = (J_1\alpha_1 + J_3\alpha_3) + (c_1\omega_1 + c_3\omega_{out}) + (M_{d1} + M_{d3}) \text{ (meshing phase)} \\ M_{in2} = J_2\alpha_2 + (c_2 + c_3)\omega_{out} + M_{d2} \end{cases} \tag{3}$$

$$\begin{cases} M_{in1} = J_1\alpha_1 + c_1\omega_1 + M_{d1} \text{ (overrunning phase)} \\ 0 = J_3\alpha_3 + c_3\omega_{out} + M_{d3} \text{ (overrunning phase)} \\ M_{in2} = J_2\alpha_2 + (c_2 + c_3)\omega_{out} + M_{d2} \end{cases} \tag{4}$$

where, $M_{in2}$ is the input torque of input shaft #2, $\alpha_1$, $\alpha_2$ and $\alpha_3$ are the angular accelerations of input shaft #1, input shaft #2 and output shaft, respectively, $J_2$ is equivalent moment of the tidal-driving components, $c_1$ and $c_2$ are the viscous damping coefficients of the wave-driving components and tidal-driving components, $c_3$ is the electrical damping coefficient of the generator, and $M_{d2}$ is damping torque of the input shaft #2. In the damping torque $M_{d3}$, the electrical damping torque $M_e$ of the generator constitutes a significant portion, being proportional to the output angular velocity.

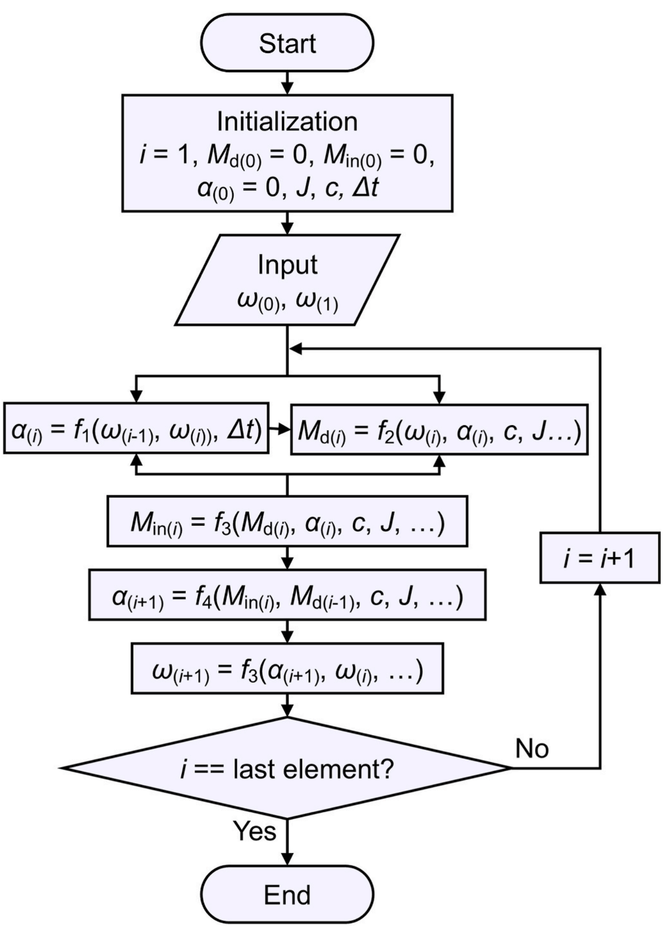


**Fig. 4.** Flowchart of the discretization modeling method.

$$\begin{cases} M_e = c_3\omega_{out} = \dfrac{k_t k_e \omega_{out}}{R} \\ U = k_e\omega_{out}\cdot\dfrac{R_{ex}}{R_{ex} + R_{in}} \end{cases} \tag{5}$$

where $k_t$ and $k_e$ are the torque coefficient and the back electromotive voltage coefficient of the generator, $U$ is the output voltage in the purely resistive load circuit, which includes the internal resistance $R_{in}$ and the external load $R_{ex}$.

## 4. Simulation

The simulation based on the proposed discretization modeling method is implemented in MATLAB. The input force and torque are computed using Eqs. (3)–(5), the output voltage is derived from Eq. (5), and the nonlinear response is determined by the boundary conditions defined in Eqs. (1) and (2). A time step of $\Delta t = 0.005$ s is employed to discretize the input velocity functions, for the balance between computational efficiency and accuracy. The equivalent Coulomb friction force is specified as a constant of 0.08 N m. Hysteresis is manifested as viscous damping, with a damping coefficient of 12.0 N s/m. The backlash in the gear transmission, reflected in the experiment results as a sawtooth fluctuation, has been considered within the error range.

### 4.1. Comparison with single ocean energy converters

In order to verify the coupling effect between wave and tidal energy, the HWTEC is compared with single energy converters following the controlled-variable method, by setting the wave and tidal inputs to 0 separately to simulate a single wave energy converter and a single tidal energy converter with the same prototype dimensions (Fig. 5). The key specifications of the HWTEC prototype are listed in Table 1, which are also used in experiments.

The wave frequency $f_w$ is set to 0.6 Hz, based on the wave data from National Data Buoy Center (Station 62050-E1, 50.0N 4.4W) on May 17, 2024, with the wave height $H_w$ of 100 mm, scaled from the prototype. When the rotation speed $\omega_t$ of tidal energy turbine is 60 rpm, the duration of overrunning phase in the single wave energy converter and the HWTEC is close (Fig. 5a), while the HWTEC demonstrates increased input force and torque (Fig. 5b) due to mutual enhancement of the damping forces between the tidal and wave energy capture modules. The output voltage of HWTEC is equal to the sum voltage of single wave energy converter and single tidal energy converter in meshing phase, but is lower in the overrunning phase (Fig. 5c). At a higher rotation speed of 120 rpm, the duration of the overrunning phase in the HWTEC is shorter than that of the single wave energy converter (Fig. 5e). Hence, it can be preliminarily inferred that the hybridization of wave and tidal energy not only couples the output power, raising the minimum output voltage (Fig. 5d and h), but also couples the mechanical damping, thereby shortening the overrunning phase (Fig. 5c and g). In other words, by integrating wave and tidal energy, the HWTEC leverages their complementary to enhance both output power and voltage smoothness, although a slight reduction in efficiency is observed due to the damping coupling.

### 4.2. Performance of the HWTEC

In order to evaluate the performance of the HWTEC under various input conditions, simulations are conducted for wave input force, tidal input torque, angular acceleration of the output shaft and output voltage with tidal turbine speed ranging from 60 rpm to 180 rpm, wave frequency from 0.2 Hz to 1.0 Hz and wave height from 40 mm to 160 mm (Fig. 6). The above parameters are based on observational data from Station 62050-E1 and covers most typical daily sea states, including common tidal current speed of 1~2 m/s, typical wind waves of 0.05–0.3

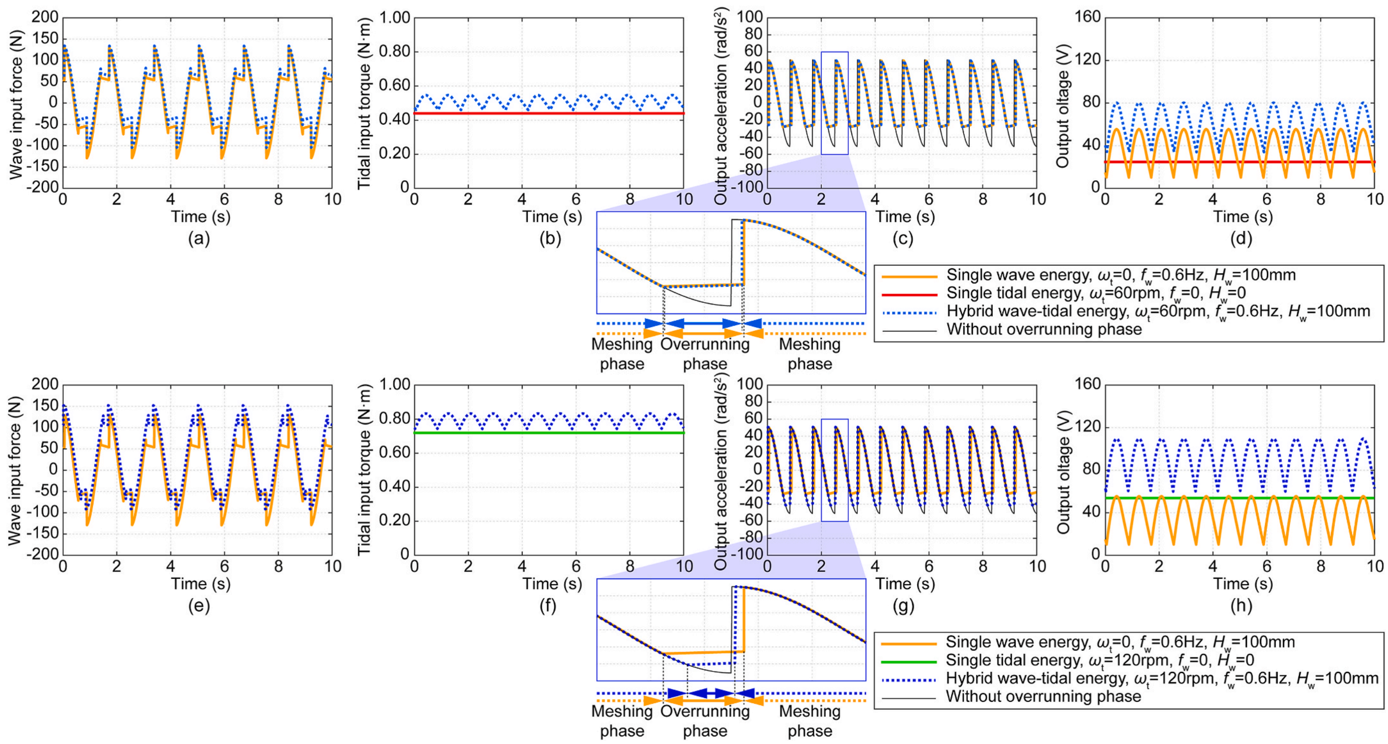

**Fig. 5.** Simulation comparison between single wave energy converter, single tidal energy converter and HWTEC.

**Table 1**
Key specifications of HWTEC prototype.

| | |
|---|---|
| Moment of inertia $J_1$ in meshing phase | $2.43 \times 10^{-3}$ kg m$^2$ |
| Moment of inertia $J_1$ in overrunning phase | $2.28 \times 10^{-3}$ kg m$^2$ |
| Moment of inertia $J_2$ | $1.02 \times 10^{-4}$ kg m$^2$ |
| Moment of inertia $J_3$ | $2.81 \times 10^{-4}$ kg m$^2$ |
| Mass of NMLRCD prototype | 9.2 kg |
| Measurements of NMLRCD prototype | H180 × L440 × W480 mm |
| Stroke of NMLRCD prototype | ±100 mm |
| External load resistance | 498.7 Ω |

Hz and short wind waves of 0.3–1.0 Hz. A rectification circuit and an external resistor of 500 Ω are connected to the generator output. At the wave frequency $f_w$ of 0.6 Hz and wave height $H_w$ of 100 mm (Fig. 6a ~ 6d), as the rotation speed $\omega_t$ of tidal turbine increases from 60 rpm to 180 rpm, the maximum tidal input torque rises from 0.546 N m to 1.111 N m (Fig. 6b). Due to the coupling damping, the maximum wave input force also increases from 130.10 N to 166.02 N (Fig. 6a), and the input torque oscillates at twice the wave frequency (Fig. 6b). The overrunning phase duration shortens from 0.30 s to 0.09 s (Fig. 6c), and the maximum output voltage increases from 79.22 V to 140.56 V (Fig. 6d). Compared to the effects of varying tidal inputs, changes in wave frequency has a more significant impact on the overrunning phase. At $\omega_t =$ 60 rpm and $H_w = 100$ mm (Fig. 6e ~ 6h), as $f_w$ increases from 0.2 Hz to 1.0 Hz, the maximum input force rises from 58.25 N to 334.95 N, while it will achieve 352.43 N if there is no overrunning phase (Fig. 6e). Corresponding maximum output voltage increases from 42.04 V to 112.02 V, and the minimum output voltage rises from 24.04 V to 53.10 V, which will remain at 24.04 V if without overrunning phase (Fig. 6h). At $f_w = 0.2$ Hz, overrunning does not occur. At 0.4 Hz, 0.6 Hz, 0.8 Hz and 1.0 Hz, the reduction in input force, the increase in input torque and the improvement in output power are separated and shown in Fig. 6e, f and 6h, respectively. The introduction of overrunning phase improves output power by 0.22 %, 1.34 %, 3.12 % and 4.73 % respectively, and also makes the output voltage smoother. For $\omega_t = 60$ rpm and $f_w = 0.6$ Hz (Fig. 6i ~ 6l), the increase of $H_w$ from 40 mm to 160 mm results in maximum input force increasing from 64.25 N to 194.20 N, maximum input torque increasing from 0.502 N m to 0.630 N m, and the output voltage increasing from 24.50 V–45.50 V–57.96 V–108.52 V.

In order to further evaluate the performance in terms of power, efficiency, output stability and the impact of varying input conditions, Fig. 7 summarizes the relevant simulation results. To quantify voltage stability and fluctuation, the ratio of minimum to maximum voltage, denoted as $\eta$, is introduced to indicate the extent of voltage fluctuation relative to the peak value. For applications such as power supply or electrolyzers of hydrogen production on offshore platforms, the stable voltage is essential, meaning a higher ratio of minimum to maximum voltage indicates improved usability and efficiency.

When the wave frequency $f_w$ is 0.6 Hz and wave height $H_w$ is 100 mm (Figs. 7a–1), increasing the rotation speed $\omega_t$ of tidal turbine from 60 rpm to 180 rpm significantly raises the tidal input power from 3.53 W to 22.48 W, while wave input power increases slightly from 8.85 W to 12.08 W. The output power rises from 6.10 W to 18.72 W, with corresponding efficiency changing from 49.26 % to 54.18 %. Specifically, both the maximum and minimum output voltages increase approximately linearly (Figs. 7b–1), leading to a steady increase in the ratio of minimum to maximum voltage. It is found that as the tidal input power increases with increasing rotation speed $\omega_t$, the coupling between the wave and the tidal energy capture modules also induces the damping force coupling, causing a slight increase in the wave input power. In terms of efficiency, the electrical damping force as the dominant component of the total system damping, varies proportionally with speed, whereas friction damping remains constant in theory and does not increase with speed. Therefore, efficiency is generally expected to increase with increasing tidal input speed. However, damping coupling shortens the overrunning phase (Figs. 7c–1), leading to a slight efficiency reduction. This reduction, however, is insufficient to outweigh the gains from higher input speeds, resulting in an overall slight increase in efficiency (Figs. 7a–1).

Similarly, in the control group for wave frequency $f_w$ (Figs. 7a–2), the wave input power rises significantly from 1.51 W to 33.69 W, while the tidal input power slightly increases from 3.33 W to 4.06 W. The output

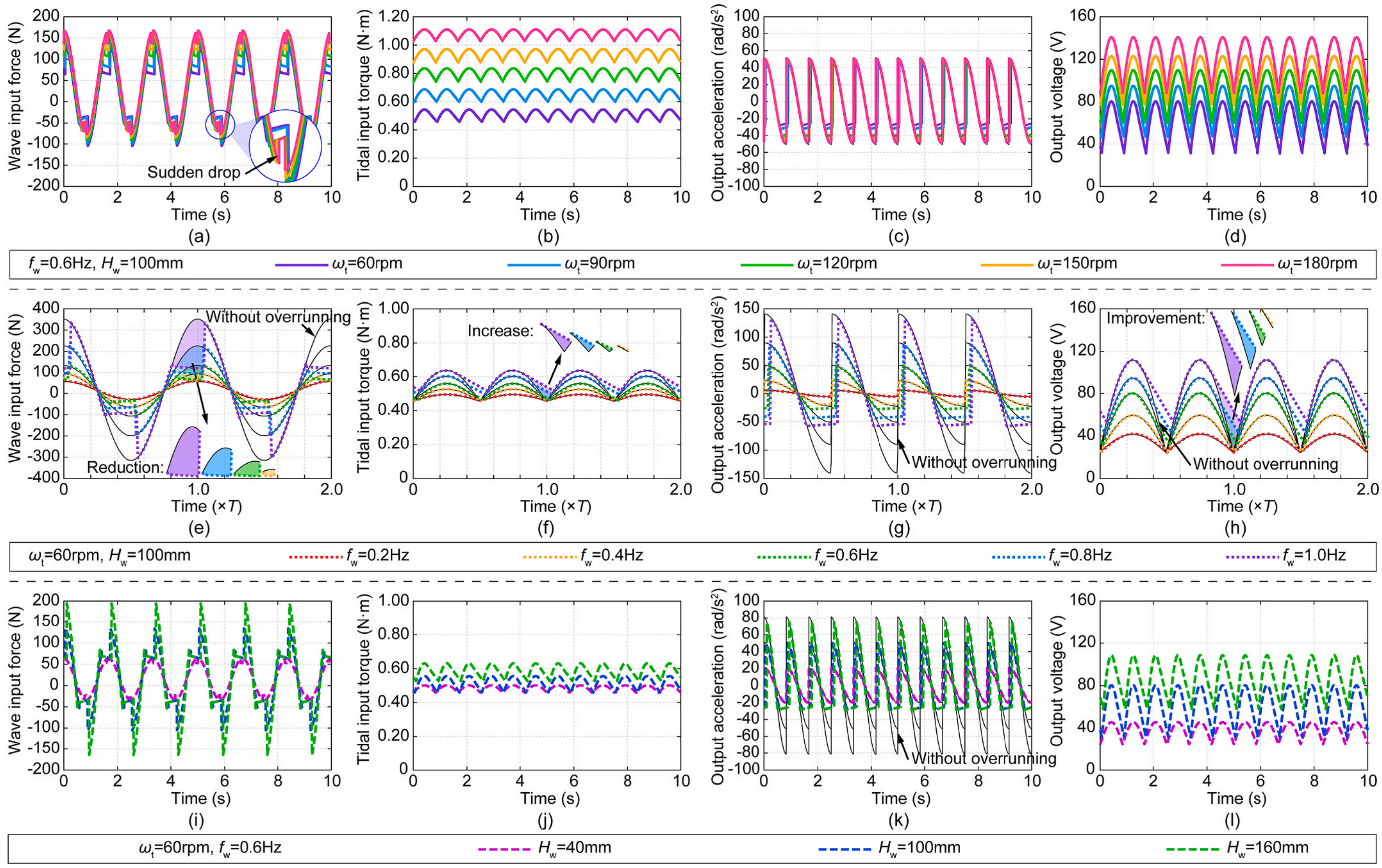


**Fig. 6.** Simulation results of input force, input torque, output acceleration and output voltage, with different input of tidal energy and wave energy.

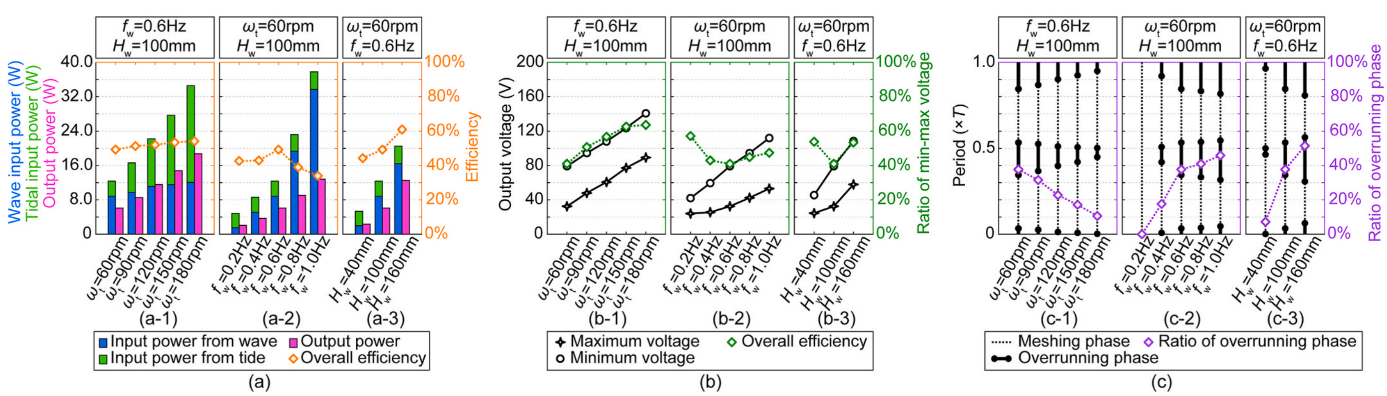


**Fig. 7.** Simulation results summary and comparison of input power, efficiency, output voltage and overrunning phase.

power changes from 2.06 W to 12.84 W. Notably, at $f_w = 0.6$ Hz, the efficiency peaks at 49.26 %, and the ratio of minimum to maximum voltage reaches the lowest value at 41.00 % (Figs. 7b–2). To explain it, the frequencies group of 0.2 Hz–1.0 Hz needs to be split into two groups. In the first group, with frequencies of 0.2 Hz, 0.4 Hz and 0.6 Hz, the overrunning phase is either extremely short or nearly absent. Even in the short overrunning phase at $f_w = 0.4$ Hz, the input force, input torque and output speed closely resemble those in cases without overrunning. It results in stable increases in both input power and output power. While without change in friction damping, the proportion of damping power in the total power decreases slightly, contributing a small increase of efficiency (Figs. 7a–2). The minimum output voltage increases slightly since the overrunning phase is insignificant, while the maximum voltage still increases approximately linearly, reducing the ratio of minimum to maximum voltage significantly (Figs. 7b–2). In the second group, with frequencies of 0.6 Hz, 0.8 Hz and 1.0 Hz as a group, the overrunning phase grows more significant with increasing frequency, leading to the noticeable rise in minimum output voltage and consequently the higher ratio of minimum to maximum voltage (Figs. 7b–2). Although the introduction of overrunning phase partially utilizes inertia to enhance the output power, the input rack, rigidly connected to the buoy, still reciprocates. Its inertia in the reciprocation results in significant energy loss and reduces efficiency under high frequency and large acceleration (Figs. 7a–2).

The effect of changing wave height on power and efficiency is relatively straightforward. As wave height $H_w$ increases from 40 mm to 160 mm (Figs. 7a–3), wave input power rises from 1.96 W to 16.44 W, while tidal input power grows modestly from 3.37 W to 4.08 W. The output power increases from 2.36 W to 12.51 W. The efficiency, calculated as the ratio of output power to total input power, increases from 44.28 % to 60.94 %, accompanied by a notable extension of the overrunning phase due to the rise in wave height. Here, comparison of the acceleration data in Fig. 6g and k reveals that while the acceleration increases as the wave height increases to 160 mm, it remains well below the acceleration at $f_w$ = 1.0 Hz, hence the decrease of efficiency in the frequencies group is not observed. In terms of voltage (Figs. 7b–3), when $H_w$ is 40 mm, the overrunning phase comprises only 7.2 % of each cycle (Figs. 7c–3), making tidal energy the primary determine the minimum voltage. And the voltage contribution from wave energy is minimal, so the maximum value is also low, resulting in the large ratio of minimum to maximum voltage of 53.85 %. While at wave height of 100 mm and 160 mm, wave energy input begins to dominate, and with the overrunning phase expanding to 37.73 % and 51.46 %, respectively (Figs. 7c–3). Consequently, the ratio of minimum to maximum voltage increases from 41.00 % to 53.41 % as the wave height rises (Figs. 7b–3).

Simulation results also indicate that minor disturbances in the tidal input speed can cause notable fluctuations in input torque. Although the overrunning mechanism helps to mitigate these fluctuations, its effectiveness remains constrained. Moreover, the model simplifies friction and viscous damping as constants and linear functions, respectively, which leads to the growing error between simulation and experimental results as input velocity rises.

Wave and tidal inputs are simulated using the pseudo real-time wave (PRTW) approach proposed in Ref. [41] (Fig. 8a), according to the real wave data from National Data Buoy Center (Station 62050-E1, 50.0N 4.4W) and emphasizing wave height, wave frequency and wavelength in the whole day. The wave frequency ranges approximately from 0.01 to 1.0 Hz, with a significant wave height of 1.0–1.6 m and a dominant wave period of 2~6 s. The tidal turbine operates at a constant speed of 60 rpm. Successfully integrating random wave inputs into the HWTEC simulation, the input force and torque acting on the HWTEC (Fig. 8b), as well as the output voltage (Fig. 8c), are obtained.

When the wave input velocity reaches 2.5 m/s and the load resistance is 1.2 kΩ, the average input and output powers are 377.4 W and 98.7 W, respectively, with the output voltage peaking at 397.2 V. An overall efficiency of 26.2 % is achieved. The introduction of the overrunning phase increases the ratio of minimum to maximum voltage from 0.32 to 0.53. For comparison, a study on a single wave energy converter of similar scale [42] reported an increase in this ratio from 0 to 0.43 due to the overrunning phase. In the present case, the overrunning phase enhances the average output voltage by 32.2 % and the average output power by 21.3 %, while significantly mitigating the efficiency loss caused by damping coupling. Although the average efficiency of current tidal energy converters under real sea conditions ranges from 35 % to 40 %, and wave energy converters range from 20 % to 45 % [17], the hybrid wave-tidal energy strategy demonstrates a distinct advantage in improving output voltage stability rather than efficiency. Particularly, it enhances the lower bound of the voltage range. The overrunning phase further reduces extreme voltage fluctuations. These findings verify that the hybrid wave-tidal strategy contributes meaningfully to enhancing output stability and power, confirm the compatibility of the discretization modeling method with discrete real wave inputs, and offer a methodological basis and reference for future wave tank and marine field tests.

## 5. Experiments

### 5.1. Experiment setup

A dual-input test bench, powered by two servo motors, is constructed to evaluate the performance of the HWTEC in laboratory (Fig. 9). Servo motor #1 operates in a sinusoidal motion with the frequency of $f_w$ and amplitude of ($H_w/2$), driving the reciprocating rack through a rack-pinion mechanism to simulate wave energy input. Servo motor #2 rotates continuously to simulate tidal energy input. The electrical output is routed through a rectifier and resistor, with voltage measured via an oscilloscope. Force sensors and torque sensors are deployed between the rack-pinion mechanism and the NLMRCD, between servo motor #2 and the NLMRCD, and between the NLMRCD and the generator, in order to measure the input force, input torque and output force. Data from all sensors are collected by the computer through data acquisition cards. Adjustable bases are employed to support and align all the above components, enhancing assembly precision and transmission efficiency.

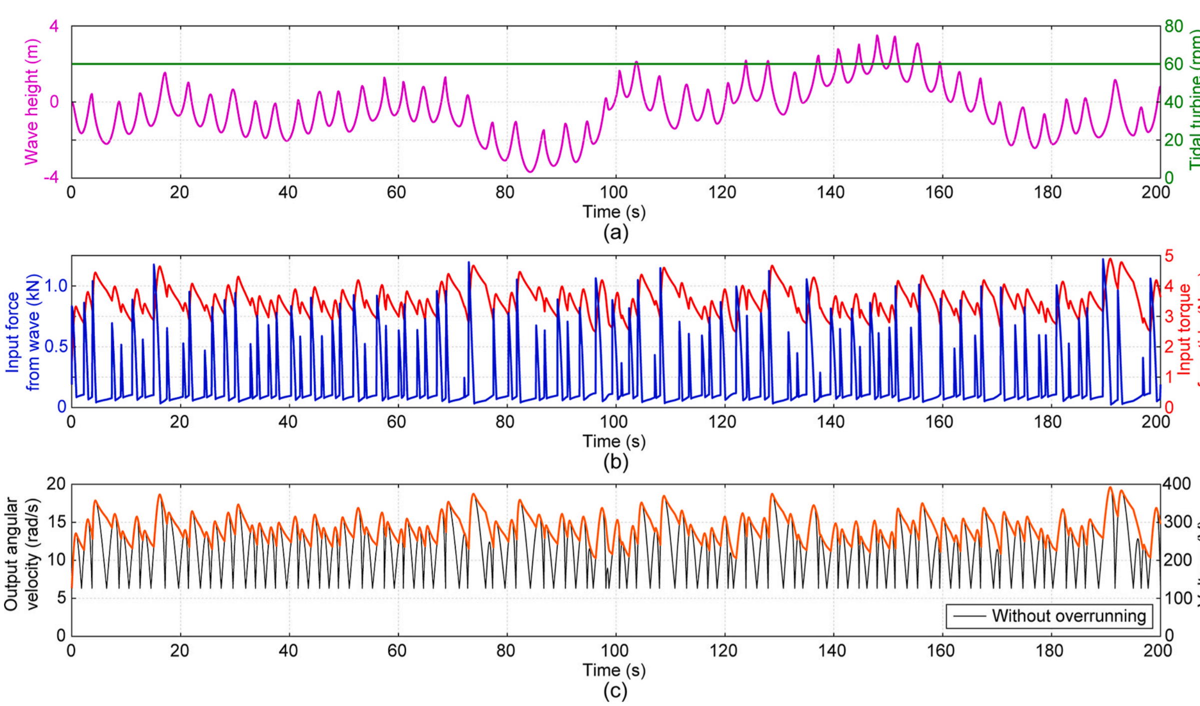


**Fig. 8.** Predictive simulation based on pseudo real-time wave (PRTW).

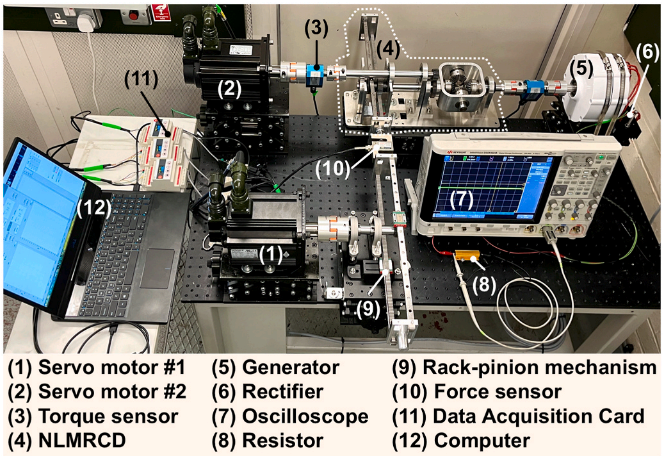


**Fig. 9.** Setup of dual-input test bench for wave-tidal energy lab experiment.

### 5.2. Results and discussion

The lab experiments are conducted under the identical input conditions as the simulations to validate the modeling method (Fig. 10). To minimize errors caused by shocks and variable damping during startup, all experimental data are recorded only after the system reaches steady-state operation.

For the experimental conditions where $f_w = 0.6$ Hz, $H_w = 100$ mm and $\omega_t$ values of 60 rpm, 90 rpm, 120 rpm, 150 rpm and 180 rpm, the maximum wave input forces are 133.50 N, 150.00 N, 164.56 N, 167.96 N and 173.79 N, respectively (Fig. 10a). Corresponding maximum tidal input torques are 0.575 N m, 0.717 N m, 0.874 N m, 0.996 N m and 1.126 N m (Fig. 10b), with maximum output voltages of 82.01 V, 97.29 V, 112.96 V, 129.21 V and 143.13 V, respectively (Fig. 10c). When $\omega_t =$ 60 rpm, $H_w = 100$ mm and $f_w$ values of 0.2 Hz, 0.4 Hz, 0.6 Hz, 0.8 Hz and 1.0 Hz, the maximum wave input forces are 59.22 N, 89.32 N, 133.50 N, 245.63 N and 366.02 N, respectively (Fig. 10d). Corresponding maximum tidal input torques are 0.537 N m, 0.566 N m, 0.575 N m, 0.641 N m and 0.675 N m (Fig. 10e), with maximum output voltages of 45.07 V, 63.44 V, 82.01 V, 101.55 V and 118.18 V, respectively (Fig. 10f). For $\omega_t = 60$ rpm, $f_w = 0.6$ Hz and $H_w$ values of 40 mm, 100 mm and 160 mm, the maximum wave input forces are 64.56 N, 133.50 N and 200.00 N, respectively (Fig. 10g). Corresponding maximum tidal input torques are 0.519 N m, 0.575 N m and 0.650 N m (Fig. 10h), with maximum output voltages of 56.26 V, 82.01 V and 112.57 V, respectively (Fig. 10i). Overrunning phases are observed in the experiments, and the numerical trends in input force, input torque, and output voltage closely align with the simulation results. Considering unavoidable mechanical system errors and data acquisition noise, the above outcomes can be accepted as the validation of the simulation.

Fig. 10 summarizes the input power, output power, efficiency, output stability, and the effects of various input conditions based on the experimental results. The experimental results for wave and tidal input powers, output power, and efficiency (Fig. 11a) closely align with the corresponding simulation outcomes presented in Fig. 7, indicating good consistency between the physical test and model prediction. This comparison confirms the reliability of the proposed discretization modeling method. However, it is noticed that the maximum voltages observed experimentally in Fig. 11b are generally higher than those in the simulation (Fig. 7b), mainly due to voltage measurement noise. Likewise, the experimentally observed minimum voltages tend to be lower, leading to a reduced ratio of minimum to maximum voltage in Fig. 11b. These errors are further explained by the sawtooth fluctuations observed in the voltage curve (Fig. 10), which result from mechanical inaccuracies and sensor noise during data acquisition. Overall, the experimental trends align well with the simulated behavior, while deviations can be attributed to identifiable real-world factor. It significantly increases the standard deviation of the measured voltage. Consequently, the error is considered reasonable and unavoidable. Furthermore, mechanical

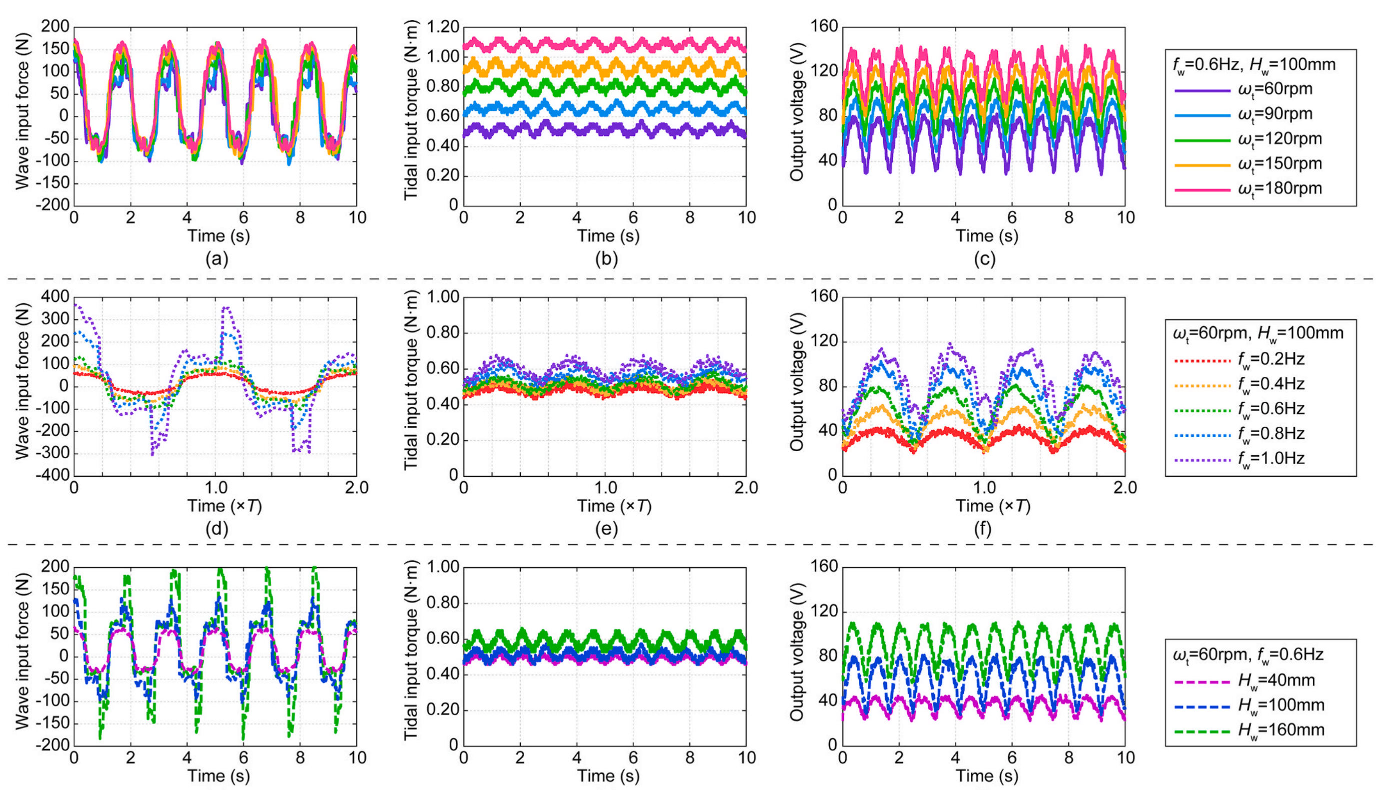


**Fig. 10.** Experiment results of input force, input torque and output voltage, with different input of tidal energy and wave energy.

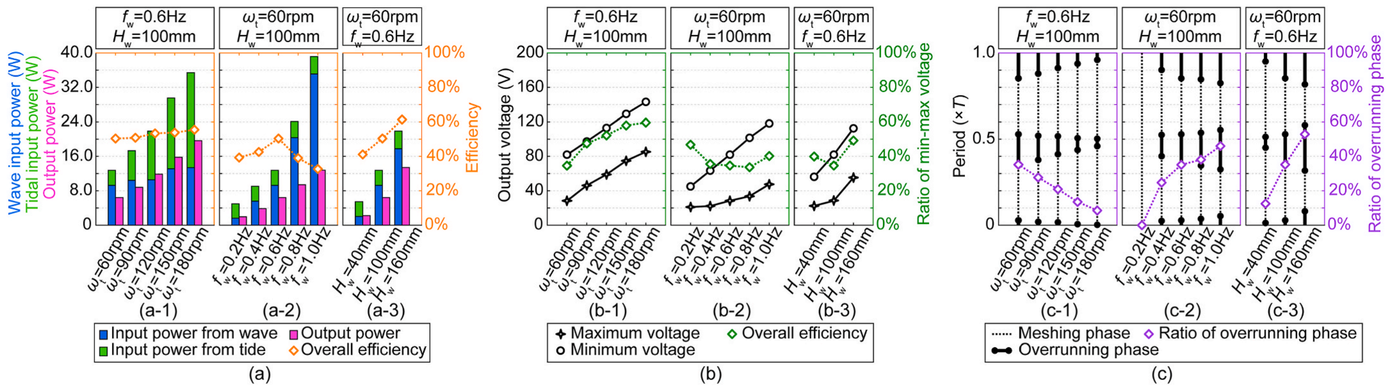


**Fig. 11.** Experiment results summary and comparison of input power, efficiency, output voltage and overrunning phase.

system errors and data acquisition noise hinder the clear identification of the overrunning and meshing phases in the experimental data. Therefore, the overrunning phase duration shown in Fig. 11c is an averaged value, obtained by fitting voltage profiles over at least five cycles and comparing them with theoretical predictions.

However, due to the absence of a more refined test platform, limitations of the dual-input test bench designed and built in this study in terms of accuracy and system control contribute to experimental errors and fluctuations. To quantitatively evaluate the consistency between simulation and experimental results, relative errors are calculated to reflect the degree of agreement. For instantaneous variables such as voltage (Fig. 10), pointwise error analysis (PEA) reveals deviations up to 20.5 %, which are primarily attributed to short-term fluctuations and noise in experimental data. In contrast, for average performance metrics such as power and efficiency (Fig. 11), aggregate error analysis (AEA) shows that relative errors generally remain within 5.5 %, and only reach up to 11 % in occasional extreme cases. These error metrics demonstrate that, despite certain transient discrepancies, the simulation model provides an accurate representation of the system's average behavior. The comparative analysis reinforces the validity of the modeling approach under realistic operating conditions. The presence of mechanical imperfections makes it challenging to accurately predict friction and viscous damping under experimental conditions, thereby significantly compromising accuracy. In conclusion, the HWTEC experiments conducted with the dual-input test bench demonstrate good performance, validating both the discretization modeling methodology and the simulation results effectively.

## 6. Conclusion

A Hybrid Wave-Tidal Energy Converter (HWTEC) based on Nonlinear Motions Rectification and Coupling Device (NLMRCD) is developed to enhance output power and voltage stability by leveraging the complementary between wave and tidal energy. A discretization modeling method is proposed, incorporating the coupling effects between the wave and tidal energy capture modules and accounting for the nonlinear response in the NLMRCD. A prototype is manufactured, and tested on the dual-input test bench designed in this study.

The NLMRCD, as the core component of the system, integrates a mechanical motion rectifier (MMR) and a bevel gearbox with one-way clutches. The MMR converts the reciprocating wave motion into one-way rotation, reducing energy loss during frequent directions switches. The overrunning during the rectification enhances both power output and voltage smoothness. The bevel gearbox ensures continuous energy conversion through wave-tidal coupling.

The proposed discretization modeling method treats input velocity as point data, automatically defining boundary conditions for the overrunning phase, thus simplifying voltage output solutions. Unlike previous models relying on idealized sine wave inputs, it accepts real ocean wave data. Simulations demonstrate that the introduction of overrunning phase improves output smoothness and stability. Under simulated ocean conditions, the HWTEC prototype achieves 18.72 W output, 60.94 % efficiency, and the ratio of minimum to maximum voltage of 63.56 %. It effectively increases the lower limit and smoothness of the output voltage, making it possible to utilize intermittent ocean energy for power supply or hydrogen production on offshore platforms.

A dual-input test bench is designed. Experiments conducted on the dual-input test bench corroborate the simulations, with output power reaching 19.65 W and efficiency of 61.34 %. The introduction of the overrunning phase and the coupling effect of wave-tidal energy effectively narrows the ratio of minimum to maximum voltage to 33.14 %–59.59 %, with acceptable noise and mechanical shock errors.

Due to the simplified treatment of friction and viscous damping in the modeling, simulation errors trend to increase when input speed varies significantly. Future work should focus on refining the mechanical damping model to enhance overall accuracy. The proposed modeling approach has been verified to simulate device performance using discrete point data. In subsequent research, simulations incorporating actual wave and tidal current data inputs are recommended. Additionally, since the current dual-input test bench lacks the capability to generate arbitrary wave inputs, future experiments under near-real ocean conditions will provide more comprehensive validation.

## CRediT authorship contribution statement

**Peihao Chen:** Writing – review & editing, Writing – original draft, Visualization, Validation, Software, Methodology, Investigation, Formal analysis, Data curation, Conceptualization. **Dawei Wu:** Writing – review & editing, Supervision, Resources, Project administration, Funding acquisition, Formal analysis. **Yiqing Yang:** Supervision, Resources, Project administration, Funding acquisition, Formal analysis. **Yan Zhang:** Writing – review & editing, Visualization, Formal analysis. **Athanasios Tsolakis:** Supervision, Resources, Project administration, Funding acquisition. **Karl Dearn:** Supervision, Resources, Project administration, Funding acquisition.

## Declaration of competing interest

The authors declare that they have no known competing financial interests or personal relationships that could have appeared to influence the work reported in this paper.

## Acknowledgements

The authors are thankful for the financial support from the EPSRC (the Engineering and Physical Sciences Research Council) of the United Kingdom via the research project EP/X038823/2, and Fundamental

Research Funds for the Central Universities (Grant No. JKF-20240570) of P. R. China.

## Appendix A. Supplementary data

Supplementary data to this article can be found online at https://doi.org/10.1016/j.energy.2025.138880.

Nomenclature

| | |
|---|---|
| $n$ | transmission ratio in the NLMRCD |
| $t$ | time, s |
| $v_w$ | velocity of buoy under wave driving, m/s |
| $\omega_{in1}$ | angular velocity of input shaft #1, rad/s |
| $\omega'_{in1}$ | intermediate variable related to $\omega_{in1}$, rad/s |
| $\omega_{in2}$ | angular velocity of input shaft #2, rad/s |
| $\omega_{out}$ | angular velocity of the output shaft, rad/s |
| $M_{in1}$ | input torque of the input shaft #1, N·m |
| $M_{d1}$ | damping torque of the wave-driving components, N·m |
| $J_1$ | inertia of the wave-driving components, kg·m$^2$ |
| $M_{mid}$ | torque transmitted from one-way gears to input shaft #1 |
| $M_{d3}$ | damping torque of the wave-driven components, N·m |
| $J_3$ | equivalent moment of inertia of the wave-driven components, kg·m$^2$ |
| $M_{in2}$ | input torque of the input shaft #2, N·m |
| $\alpha_1$ | angular acceleration of input shaft #1, rad/s$^2$ |
| $\alpha_2$ | angular acceleration of input shaft #2, rad/s$^2$ |
| $\alpha_3$ | angular acceleration of output shaft, rad/s$^2$ |
| $J_2$ | equivalent moment of the tidal-driving components, kg·m$^2$ |
| $M_{d2}$ | damping torque of input shaft #2, N·m |
| $c_1$ | viscous damping coefficient of the wave-driving components, N·s |
| $c_2$ | viscous damping coefficient of the tidal-driving components, N·s |
| $c_3$ | electrical damping coefficient of the generator, N·s |
| $M_e$ | electrical damping torque of the generator, N·m |
| $k_t$ | torque coefficient of the generator, V·s |
| $k_e$ | back electromotive voltage coefficient, V·s/rad |
| $U$ | output voltage, V |
| $R_{in}$ | internal resistance, Ω |
| $R_{ex}$ | external load resistance, Ω |
| $f_w$ | wave frequency, Hz |
| $H_w$ | wave height, m |
| $\omega_t$ | rotation speed of tidal turbine, rpm |
| $\eta$ | ratio of minimum to maximum voltage |

## Data availability

Data will be made available on request.

## References


[1] Roy A, Auger F, Dupriez-Robin F, Bourguet S, Tran QT. Electrical power supply of remote maritime areas: a review of hybrid systems based on marine renewable energies. Energies 2018;11(7):1904. https://doi.org/10.3390/en11071904.

[2] Chen P, Wu D. A review of hybrid wave-tidal energy conversion technology. Ocean Eng 2024;303:117684. https://doi.org/10.1016/j.oceaneng.2024.117684.

[3] Khan N, Kalair A, Abas N, Haider A. Review of ocean tidal, wave and thermal energy technologies. Renew Sust Energ Rev 2017;72:590–604. https://doi.org/10.1016/j.rser.2017.01.079.

[4] Gallutia D, Tahmasbi-Fard M, Gutierrez Soto M, He J. Recent advances in wave energy conversion systems: from wave theory to devices and control strategies. Ocean Eng 2022;252:111105. https://doi.org/10.1016/j.oceaneng.2022.111105.

[5] Widén J, Carpman N, Castellucci V, Lingfors D, Olauson J, Remouit F, et al. Variability assessment and forecasting of renewables: a review for solar, wind, wave and tidal resources. Renew Sust Energ Rev 2015;44:356–75. https://doi.org/10.1016/j.rser.2014.12.019.

[6] Dallavalle E, Zanuttigh B, Contestabile P, Giuggioli A, Speranza D. Improved methodology for the optimal mixing of renewable energy sources and application to a multi-use offshore platform. Renew Energy 2023;210:575–90. https://doi.org/10.1016/j.renene.2023.03.099.

[7] Ramli MA, Mustapa MA, Rozali RH, Azrulhisham EA. Hydrodynamic performance of heaving motion on cylinder and conical two-body point absorber in low wave energy. IOP Conf Ser Earth Environ Sci 2022;1046(1):012010. https://doi.org/10.1088/1755-1315/1046/1/012010.

[8] Zheng C-w, Pan J, Li J-x. Assessing the China sea wind energy and wave energy resources from 1988 to 2009. Ocean Eng 2013;65:39–48. https://doi.org/10.1016/j.oceaneng.2013.03.006.

[9] Rehman S, Alhems LM, Alam MM, Wang L, Toor Z. A review of energy extraction from wind and ocean: technologies, merits, efficiencies, and cost. Ocean Eng 2023;267:113192. https://doi.org/10.1016/j.oceaneng.2022.113192.

[10] Cui L, Amani S, Gabr M, Kumari WGP, Ahmed A, Ozcan H, et al. Synergistic hybrid marine renewable energy harvest system. Energies 2024;17(5):1240. https://doi.org/10.3390/en17051240.

[11] Azam A, Ahmed A, Yi M, Zhang Z, Zhang Z, Aslam T, et al. Wave energy evolution: knowledge structure, advancements, challenges and future opportunities. Renew Sust Energ Rev 2024;205:114880. https://doi.org/10.1016/j.rser.2024.114880.

[12] Al Shami E, Zhang R, Wang X. Point absorber wave energy harvesters: a review of recent developments. Energies 2019;12(1):47. https://doi.org/10.3390/en12010047.

[13] Zhang J, Yu H, Chen M. Direct-drive wave energy conversion with linear generator: a review of research status and challenges. IET Renew Power Gener 2022;17(4):1020–34. https://doi.org/10.1049/rpg2.12637.

[14] Hu H, Xue W, Jiang P, Li Y. Bibliometric analysis for ocean renewable energy: an comprehensive review for hotspots, frontiers, and emerging trends. Renew Sust Energ Rev 2022;167:112739. https://doi.org/10.1016/j.rser.2022.112739.

[15] Khare V, Bhuiyan MA. Tidal energy-path towards sustainable energy: a technical review. Clean Energy Syst 2022;3:100041. https://doi.org/10.1016/j.cles.2022.100041.

[16] Yin X, Zhao X, Zhang W. A novel hydro-kite like energy converter for harnessing both ocean wave and current energy. Energy 2018;158:1204–12. https://doi.org/10.1016/j.energy.2018.03.121.

[17] Silva RN, Nunes MM, Oliveira FL, Oliveira TF, Brasil ACP, Pinto MSS. Dynamical analysis of a novel hybrid Oceanic tidal-wave energy converter system. Energy 2023;263:125933. https://doi.org/10.1016/j.energy.2022.125933.

[18] Calheiros-Cabral T, Clemente D, Rosa-Santos P, Taveira-Pinto F, Ramos V, Morais Y, et al. Evaluation of the annual electricity production of a hybrid breakwater-integrated wave energy converter. Energy 2020;213:118845. https://doi.org/10.1016/j.energy.2020.118845.

[19] Jiang B, Li X, Chen S, Xiong Q, Chen B-f, Parker RG, et al. Dynamics of a hybrid wave-current energy converter with a novel power take-off mechanism. Active and passive smart structures and integrated systems XIII. Proc SPIE 2019;10967. https://doi.org/10.1117/12.2514186.

[20] Jiang B, Li X, Chen S, Xiong Q, Chen B-f, Parker RG, et al. Performance analysis and tank test validation of a hybrid ocean wave-current energy converter with a single power takeoff. Energy Conv Manag 2020;224:113268. https://doi.org/10.1016/j.enconman.2020.113268.
[21] Chen S, Jiang B, Li X, Xiong Q, Huang J, Zuo L. Design and dynamics of hybrid wave and current energy converter. Proceedings of the ASME design engineering technical conference, vol. 8. California, USA: Anaheim; 2019 Aug 18-21. https://doi.org/10.1115/DETC2019-98040.
[22] Chen S, Jiang B, Li X, Huang J, Wu X, Xiong Q, et al. Design, dynamic modeling and wave basin verification of a hybrid wave-current energy converter. Appl Energy 2022;321:119320. https://doi.org/10.1016/j.apenergy.2022.119320.
[23] Park M-S, Lee S-H, Ko S-C. Experimental capture width ratio on unit module system of hybrid wave energy converter for nearshore. Appl Sci 2022;12(12):5845. https://doi.org/10.3390/app12125845.
[24] Cheng Y, Dai S, Dai S, Ji C, Collu M, Yuan Z, et al. Energy conversion and hydrodynamic analysis of multi-degree-of-freedom wave energy converters integrated into a semi-submersible platform. Energy Conv Manag 2022;252:115075. https://doi.org/10.1016/j.enconman.2021.115075.
[25] Fang H, Wei Y, Feng Y. Investigation of a double-degree-of-freedom wave energy converter. Energy Rep 2020;6:402–6. https://doi.org/10.1016/j.egyr.2020.11.223.
[26] Gao H, Yu Y. The dynamics and power absorption of cone-cylinder wave energy converters with three degree of freedom in irregular waves. Energy 2018;143:833–45. https://doi.org/10.1016/j.energy.2017.11.036.
[27] Zhang C, Li D, Ding Z, Liu Y, Cao F, Ning D. Wave energy converter with multiple degrees of freedom for sustainable repurposing of decommissioned offshore platforms: an experimental study. Appl Energy 2024;376:124204. https://doi.org/10.1016/j.apenergy.2024.124204.
[28] Lu H, Xi D, Ma X, Zheng S, Huang C, Wei N. Hybrid machine learning models for predicting short-term wave energy flux. Ocean Eng 2022;264:112258. https://doi.org/10.1016/j.oceaneng.2022.112258.
[29] Eid T, Hashem H, Yetgin D, Alkhaledi A, Tutar M. Optimization and machine learning analysis of a small-scale oscillating water column (OWC) in regular waves: a computational study. Renew Sustain Energy Rev 2025;215:115577. https://doi.org/10.1016/j.rser.2025.115577.
[30] Shadmani A, Nikoo MR, Gandomi AH, Chen M. An optimization approach for geometry design of multi-axis wave energy converter. Energy 2024;301:131714. https://doi.org/10.1016/j.energy.2024.131714.
[31] Teixeira-Duarte F, Rosa-Santos P, Taveira-Pinto F. Multi-objective optimization of co-located wave-wind farm layouts supported by genetic algorithms and numerical models. Renew Energy 2025;241:122362. https://doi.org/10.1016/j.renene.2025.122362.
[32] Jiang X, Cao F, Shi H, Zhu K, Zhang C. Optimization of pendulum-based wave energy converter through mathematical approximation. Appl Energy 2025;378(A):124754. https://doi.org/10.1016/j.apenergy.2024.124754.
[33] Li X, Chen C-A, Li Q, Xu L, Liang C, Ngo K, et al. A compact mechanical power take-off for wave energy converters: design, analysis, and test verification. Appl Energy 2020;278:115459. https://doi.org/10.1016/j.apenergy.2020.115459.
[34] Martin D, Li X, Chen C-A, Thiagarajan K, Ngo K, Parker R, et al. Numerical analysis and wave tank validation on the optimal design of a two-body wave energy converter. Renew Energy 2020;145:632–41. https://doi.org/10.1016/j.renene.2019.05.109.
[35] Li X, Chen C-A, Chen S, Xiong Q, Huang J, Lambert S, et al. Dynamic characterization and performance evaluation of a 10-kW power take-off with mechanical motion rectifier for wave energy conversion. Ocean Eng 2022;250:110983. https://doi.org/10.1016/j.oceaneng.2022.110983.
[36] Chen P, Yang Y. Design, dynamics modeling, and experiments of a vibration energy harvester on bicycle. IEEE ASME Trans Mechatron 2023;28(5):2670–8. https://doi.org/10.1109/TMECH.2023.3246516.
[37] Stavropoulou C, Katsidoniotaki E, Faedo N, Göteman M. Multi-fidelity surrogate modeling of nonlinear dynamic responses in wave energy farms. Appl Energy 2025;380:125011. https://doi.org/10.1016/j.apenergy.2024.125011.
[38] Hiron L, Schönau MC, Raja KJ, Chassignet EP, Buijsman MC, Arbic BK, et al. The influence of vertical resolution on internal tide energetics and subsequent effects on underwater acoustic propagation. J Adv Model Earth Syst 2025;17(1):e2024MS004389. https://doi.org/10.1029/2024MS004389.
[39] Luo M, Su X, Kazemi E, Jin X, Khayyer A. Review of smoothed particle hydrodynamics modeling of fluid flows in porous media with a focus on hydraulic, coastal, and ocean engineering applications. Phys Fluids 2025;37:021303. https://doi.org/10.1063/5.0252125.
[40] Bao L, Wang Y, Chen J, Li H, Jiang C, Zhuo Y, et al. Research on hydrodynamic performance of S-type turbine based on linear wave. PLoS One 2025;20(1):e0310478. https://doi.org/10.1371/journal.pone.0310478.
[41] Chen P, Wu D, Yang Y, Tsolakis A. Discretization modeling with pseudo real-time waves input of the hybrid wave-tidal energy converter based on non-linear motions rectification and coupling device. Energy 2025;323:135615. https://doi.org/10.1016/j.energy.2025.135615.
[42] Yang Y, Chen P, Liu Q. A wave energy harvester based on coaxial mechanical motion rectifier and variable inertia flywheel. Appl Energy 2021;302:117528. https://doi.org/10.1016/j.apenergy.2021.117528.
[43] Wu B, Zhan M, Wu R, Zhang X. The investigation of a coaxial twin-counter-rotating turbine with variable-pitch adaptive blades. Energy 2023;267:126546. https://doi.org/10.1016/j.energy.2022.126546.